

# A local quantized marker for topological magnons from circular dichroism

Baptiste Bermond,<sup>1,\*</sup> Anaïs Defossez,<sup>1,2,3,†</sup> and Nathan Goldman<sup>1,2,3,‡</sup>

<sup>1</sup>Laboratoire Kastler Brossel, Collège de France, CNRS, ENS-Université PSL, Sorbonne Université, 11 Place Marcelin Berthelot, 75005 Paris, France

<sup>2</sup>International Solvay Institutes, 1050 Brussels, Belgium

<sup>3</sup>Center for Nonlinear Phenomena and Complex Systems, Université Libre de Bruxelles, CP 231, Campus Plaine, B-1050 Brussels, Belgium

(Dated: May 29, 2025)

The low-energy excitations of a spin system can display Bloch bands with non-trivial topological properties. While topological magnons can be identified through the detection of chiral propagating modes at the sample's edge, an intriguing approach would be to directly probe their topological nature via localized measurements deep within the bulk. In this work, we introduce a quantized topological marker suitable for topological spin systems, which can be experimentally accessed by combining a local driven-dissipative preparation scheme with a circular-dichroic measurement. Demonstrated on a 2D ferromagnetic Heisenberg spin system incorporating Dzyaloshinskii-Moriya interactions, this method effectively maps a local Chern marker with single-site resolution while inherently accounting for magnon losses. Our work offers a general strategy to access local topological markers in bosonic settings within a driven-dissipative framework.

*Introduction.* — Certain materials can exhibit low-energy bosonic excitations with topological band properties [1–5]. This is the case of topological magnons, which can be found in materials such as Cu[1,3-benzenedicarboxylate] [6, 7], Na<sub>3</sub>Cu<sub>2</sub>SbO<sub>6</sub> [8], β-Cu<sub>2</sub>V<sub>2</sub>O<sub>7</sub> [9], Mn<sub>5</sub>Ge<sub>3</sub> [10] and CrI<sub>3</sub> [11]. A direct manifestation of these topological properties is provided by the chiral edge excitations, which can be probed spectroscopically [12, 13]. In this context, a relevant question concerns whether one could access a quantized topological response, deep in the bulk of the system, which would directly reflect the topological nature of the magnonic Bloch bands. Besides, edge magnonic excitations have been shown to be affected by losses and dissipation [14]. It would therefore be appealing to develop a realistic scheme to access topological responses of magnonic excitations that would remain immune to such losses, i.e. within an engineered driven-dissipative scenario.

More generally, the identification of local markers of topology has been an important quest in the realm of topological quantum matter. Prime instances are provided by the so-called Bianco-Resta marker [15], and also by the local Streda response [16–20], which allows for the local determination of the (many-body) Chern number deep in the bulk of a Chern-insulating system. For topological magnon systems, the challenge is two-fold due to the charge-neutral and bosonic nature of the excitations: while Bloch bands are naturally filled in fermionic settings, by simply adjusting the chemical potential, the ground-state of bosonic systems often consists in an empty vacuum state; moreover, magnons are charge-neutral, and hence, they do not couple to traditional experimental probes of topological matter. Altogether, any strategy aimed at measuring the local topological properties of magnonic excitations must be accompanied by a well-defined preparation and probing

protocol.

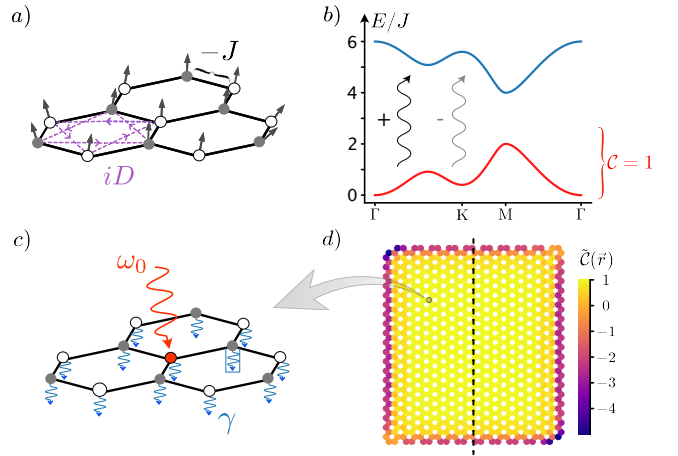


Figure 1. *Local Chern marker measurement in a topological magnon system.* (a) Illustration of the 2D spin model in Eq. (1), with nearest-neighbor ferromagnetic Heisenberg interactions  $J$  (black), and next-nearest-neighbor DM interactions  $D$  (blue). (b) The corresponding energy spectrum displays two bands, with respective Chern numbers  $\mathcal{C} = \pm 1$ ; here  $J = 2D > 0$ . (c) Sketch of the preparation scheme: a localized spin excitation is created using a local pump field at frequency  $\omega_0$ , in the presence of a homogeneous loss rate  $\gamma$ . The resulting steady state uniformly occupies the low-energy magnonic band. A circular perturbation (not shown) is then applied to drive transitions to the upper band [see panel (b)]. (d) The Chern marker, as extracted from this local circular-dichroic measurement, is shown for a  $20 \times 20$  spin system.

In this Letter, we introduce a local topological marker that can be experimentally accessed in a broad range of topological bosonic settings, such as topological magnons. Our construction consists of three steps: (i) the preparation of a localized (single-site) excitation,

deep in the bulk, which entirely projects onto a single topological band; (ii) the application of a circular drive, which acts globally on the system; (iii) the monitoring of excitation rates (or power absorbed) upon the action of the circular drive, for the two opposite orientations of the drive [21–25]. This local circular-dichroic measurement eventually provides the desired topological marker, revealing the Chern number of the underlying band at the single-site level. Importantly, the preparation step can be achieved through a driven-dissipative approach, which potentially guarantees the robustness of this approach to inevitable losses. While this construction generally applies to topological bosonic systems, we illustrate it on the concrete case of magnonic excitations in a 2D ferromagnetic Heisenberg spin system [2].

*Model and spin-wave theory.*— For concreteness, let us consider a prototypical model of topological magnon systems [2, 26]. This model consists of a ferromagnetic material with spin-orbit coupling, whose localized spins are located on a honeycomb lattice. The Hamiltonian is expressed as [Fig. 1(a)]:

$$\hat{\mathcal{H}} = -J \sum_{\langle ij \rangle} \vec{s}_i \cdot \vec{s}_j + \sum_{\langle\langle ij \rangle\rangle} \vec{D}_{ij} \cdot (\vec{s}_i \wedge \vec{s}_j), \quad (1)$$

where the spin operators  $\vec{s}_i$  describe spin-degrees of freedom. The first term of Hamiltonian (1) is a nearest-neighbor Heisenberg interaction, and we set  $J > 0$  to stabilize the ferromagnetic order. The second term is the Dzyaloshinskii–Moriya (DM) interaction between the next-nearest neighboring spins. Since the honeycomb plane is a mirror plane of the system, the DM vector does not have any in-plane component [27, 28], i.e.  $\vec{D}_{ij} = D_{ij} \vec{e}_z$ , with  $\vec{e}_z$  the unit vector in the z-direction. Considering a uniform system, we set  $D_{ij} = -D_{ji} = D\eta_{ij}$ , where the sign  $\eta_{ij} = \pm 1$  depends on the orientation of the two next-nearest spins, as shown in blue in Fig. 1(a). Interestingly, this Hamiltonian commutes with the z-component of the total spin  $\hat{S}_z = \sum_i \hat{s}_i^z$ . As a consequence, the total magnetization in the z-direction  $S_z = \langle \hat{S}_z \rangle$  is a conserved quantity, allowing one to study sectors of different magnetizations independently.

A standard way to describe magnonic excitations above an ordered ground state is to map the spin operators to bosonic operators using a so-called Holstein–Primakoff transformation [29]. It is known that the ground state of our system is a ferromagnetic ground state with a global  $SO(3)$  symmetry [14], provided that  $D$  is small enough ( $D \lesssim 0.7JS$ ). The direction can then be fixed along the z-axis, without altering the total magnetization conservation, by adding a small magnetic field along the z-axis. For such a polarized ground-state, the Holstein-Primakoff transform takes the form

$$\hat{s}_i^+ = \sqrt{2S} \sqrt{1 - \frac{\hat{a}_i^\dagger \hat{a}_i}{2S}}, \quad \hat{s}_i^- = \sqrt{2S} \hat{a}_i^\dagger \sqrt{1 - \frac{\hat{a}_i^\dagger \hat{a}_i}{2S}}, \quad (2)$$

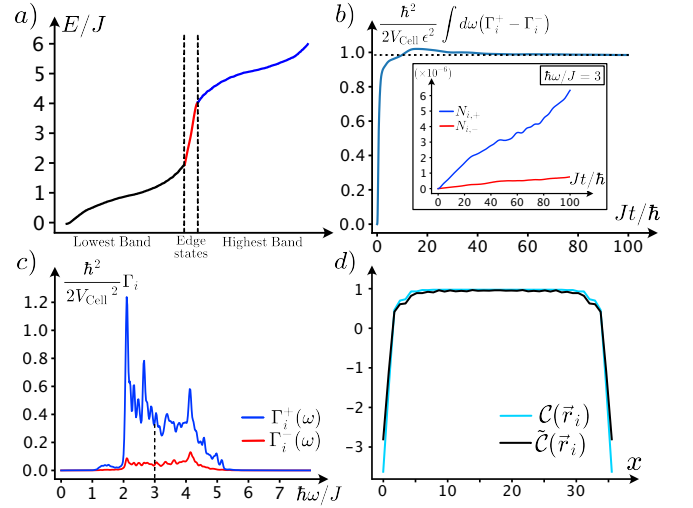


Figure 2. *Dichroism measurement for the  $S=1/2$  bosonized Hamiltonian (3).* (a) Single-magnon spectrum for a  $20 \times 20$  lattice and  $D=J/2$ : the states in the lowest (highest) bulk band are represented in black (blue), while the edge states are shown in red. (b) Time evolution of the integrated differential rate [Eq. (8)] as a function of time, for a specific initial state located in the bulk; the driving amplitude is  $\epsilon = 2.10^{-4} J/a$ . In the long-time limit, this quantity converges to a quantized value, defining a local Chern marker. The inset shows the time evolution of the excited fractions  $N_{i\pm}^{\pm}(\omega, t)$  for  $\hbar\omega/J = 3$ , corresponding to the dashed line in panel (c). (c) The late-time excitation rates  $\Gamma_{i,\pm}(\omega, Jt/\hbar = 100)$  as a function of  $\hbar\omega/J$ . (d) The Chern markers  $\mathcal{C}(\vec{r}_i)$  (blue) and  $\tilde{\mathcal{C}}(\vec{r}_i)$  (black) are evaluated along the dashed line depicted in Fig. 1(d). The local Chern markers exhibit a quantized value ( $\mathcal{C} = \tilde{\mathcal{C}} = 1$ ) in the bulk, while they take large negative values near the edges.

and  $\hat{s}_i^z = S - \hat{a}_i^\dagger \hat{a}_i$ , with  $\hat{s}_i^\pm = \hat{s}_i^x \pm i\hat{s}_i^y$  and where  $\hat{a}_i^\dagger (\hat{a}_i)$  creates (annihilates) a magnon at site  $i$ . Applying this mapping to Eq. (1), and restricting ourselves to linear spin waves [30], one obtains

$$\hat{\mathcal{H}} = -N_l JS^2 - JS \sum_{\langle ij \rangle} (\hat{a}_j^\dagger \hat{a}_i + \hat{a}_i^\dagger \hat{a}_j) + JS \sum_i z_i \hat{a}_i^\dagger \hat{a}_i + iDS \sum_{\langle\langle ij \rangle\rangle} \eta_{ij} (\hat{a}_j^\dagger \hat{a}_i - \hat{a}_i^\dagger \hat{a}_j), \quad (3)$$

with  $N_l = \sum_i z_i$  the total number of links, where  $z_i$  denotes the number of nearest neighbors of site  $i$ , i.e.,  $z_i = 3$  in the bulk, and  $z_i \leq 3$  on the edges. This Hamiltonian (3) describes a bosonic analog of the Haldane model [31], with a staggered  $\pi/2$  phase and a topological band-gap of size  $6\sqrt{3}DS$ , whose spectrum is represented in Fig. 1(b).

*A practical Chern marker for topological magnons* — Topological magnon properties can be captured at the single-magnon level. As an initial state, we thus consider a single-magnon state that uniformly occupies the lowest band of the spectrum and that is localized on a single

site of the lattice. Theoretically, such an initial state  $|\downarrow_i\rangle$  can be computed as the projection onto the lowest band of the single-magnon excitation  $|i\rangle = \hat{a}_i^\dagger |0\rangle$ , with  $|0\rangle$  the vacuum state defined by  $\hat{a}_i |0\rangle = 0$  for all site  $i$ :

$$|\downarrow_i\rangle = \frac{\sum_{g \in LB} |g\rangle \langle g|i\rangle}{\sqrt{\sum_{g \in LB} |\langle g|i\rangle|^2}}, \quad (4)$$

where  $\sum_{g \in LB}$  denotes a sum over all the eigenstates  $|g\rangle$  belonging to the lowest energy band [Fig. 2.(a)].

We will now analyze the response of this localized state to a global circular drive. We introduce this chiral perturbation in the form of a time-periodic potential

$$\delta \hat{\mathcal{H}}_{\pm}(t) = 2\epsilon [\hat{x} \cos(\omega t) \pm \hat{y} \sin(\omega t)], \quad (5)$$

where  $\hat{x}/\hat{y}$  denote the position operators defined as  $\hat{x} = \sum_j x_j \hat{a}_j^\dagger \hat{a}_j$ , with  $x_i$  the x coordinate of the site  $i$ ;  $\omega$  is the drive frequency,  $\epsilon$  is the amplitude, and  $\pm$  denotes the two drive orientations. Assuming a chiral drive of small amplitude, we evaluate the excited fraction in the higher band at first order in time-dependent perturbation theory, and we obtain

$$N_i^{\pm}(\omega, t) = \frac{\epsilon^2}{\hbar^2} \sum_{e \notin LB} \left| \sum_{g \in LB} \langle e|\hat{x} \pm i\hat{y}|g\rangle \langle g|\downarrow_i\rangle \frac{e^{it(\omega_{eg}-\omega)} - 1}{\omega_{eg} - \omega} \right|^2 \quad (6)$$

where  $\hbar\omega_{eg} = E_e - E_g$ , and  $|e\rangle$  denotes states belonging to the higher-energy band [Fig. 2.(a)]. The inset of Fig. 2(b) represents two illustrative time evolutions for  $\epsilon = 2.10^{-4}J/a$  and  $\hbar\omega = 3J$ . The circular dichroic signal is then obtained by comparing the long-time chiral excitation rates:

$$\Delta\Gamma_i(\omega, t) = \frac{N_i^+(\omega, t) - N_i^-(\omega, t)}{2t}. \quad (7)$$

Figure 2(c) represents an illustrative frequency evolution of the rates  $\Gamma_i^{\pm}(\omega, t) = N_i^{\pm}(\omega, t)/t$  for  $\epsilon = 2.10^{-4}J/a$  and  $Jt/\hbar = 100$ . Inspired by Refs. [21, 23], we consider performing a set of experiments for various frequencies of the drive  $\omega$ , and integrating the circular dichroic signal over the frequencies

$$\begin{aligned} \Delta\Gamma_i(t) &= \int d\omega \Delta\Gamma_i(\omega, t) \\ &\stackrel{t \rightarrow \infty}{=} -\frac{4\pi\epsilon^2}{\hbar^2} \text{Im} \left( \sum_{g \in LB} \langle \downarrow_i | g \rangle \langle g | \hat{x} \hat{Q} \hat{y} | g \rangle \langle g | \downarrow_i \rangle \right), \end{aligned} \quad (8)$$

with  $\hat{Q}$  the projector onto the states belonging to the higher band. Figure 2(b) represents an illustrative example of the time evolution of the integrated circular dichroic signal  $\Delta\Gamma_i(t)$  for  $\epsilon = 2.10^{-4}J/a$ . From its late time limit, we finally define a local marker  $\tilde{\mathcal{C}}(\vec{r}_i)$  as

$$\tilde{\mathcal{C}}(\vec{r}_i) = \lim_{t \rightarrow \infty} \left( \frac{\hbar^2}{V_{\text{cell}} \epsilon^2} \Delta\Gamma_i \right) \quad (9)$$

$$= -\frac{4\pi}{V_{\text{cell}}} \text{Im} \left( \sum_{g \in LB} \langle \downarrow_i | g \rangle \langle g | \hat{x} \hat{Q} \hat{y} | g \rangle \langle g | \downarrow_i \rangle \right),$$

where  $V_{\text{cell}}$  denotes the area of the unit cell. Notably, this marker closely resembles the local Chern marker introduced by Bianco and Resta [15],

$$\begin{aligned} \mathcal{C}(\vec{r}_i) &= -\frac{4\pi}{V_{\text{cell}}} \text{Im} \left( \langle \downarrow_i | \hat{P} \hat{x} \hat{Q} \hat{y} \hat{P} | \downarrow_i \rangle \right) \\ &= -\frac{4\pi}{V_{\text{cell}}} \text{Im} \sum_{g, g' \in LB} \langle \downarrow_i | g \rangle \langle g | \hat{x} \hat{Q} \hat{y} | g' \rangle \langle g' | \downarrow_i \rangle, \end{aligned} \quad (10)$$

with  $\hat{P} = \hat{\mathbb{1}} - \hat{Q}$ . However, the markers (9)-(10) differ through the off-diagonal terms of the form  $\langle g | \hat{x} \hat{Q} \hat{y} | g' \rangle$ , with  $g$  and  $g'$  two different states belonging to the lowest band. As shown in Figs. 1.(d) and 2(d),  $\tilde{\mathcal{C}}(\vec{r}_i)$  behaves like a local Chern marker: it is quantized to 1 in the bulk and large and negative near the edges. This resemblance arises because, in the bulk, the system approximates one with periodic boundary conditions, where quasimomenta  $\vec{k}$  are good quantum numbers and the lowest band states are momentum eigenstates. Since  $\hat{x} \equiv \frac{i}{\hbar} \partial_{k_x}$  is diagonal in momentum space, so is  $\hat{x} \hat{Q} \hat{y}$ , implying  $\langle g | \hat{x} \hat{Q} \hat{y} | g' \rangle = \delta_{g, g'} \langle g | \hat{x} \hat{Q} \hat{y} | g \rangle$ . After summation over  $g'$  one therefore recovers  $\tilde{\mathcal{C}}(\vec{r}_i) = \mathcal{C}(\vec{r}_i)$ . Finite-size scaling at the sample center confirms exponential convergence of both  $\tilde{\mathcal{C}}(\vec{r})$  and its finite-time version  $\tilde{\mathcal{C}}(\vec{r}, t)$  to the quantized value (see Fig.S1.a in [30]).

While these results show that integrated chiral excitation rates can probe the local Chern marker, this approach relies on two key assumptions (discussed in detail in [30]). First, the link involves a frequency integral, which, in any numerical or experimental measurement, must be approximated by a discrete sum over a finite set of frequencies [23], with spacing  $\Delta\omega$ , such that the integral in Eq. (8) is approximated by:

$$\Delta\omega \sum_{n \geq 0} \Gamma_i^+(n\Delta\omega, t) - \Gamma_i^-(n\Delta\omega, t). \quad (11)$$

This is valid for  $t < 2\pi/\Delta\omega$ , though the achievable precision depends on the number of frequency points. Second, the perturbative expression in Eq.(6) holds only for small excitation amplitudes  $\epsilon$ , ensuring  $N_{i,\pm}(\omega, t) \ll 1$  for all relevant  $\omega$  and  $t$ . Since the relationship between chiral excitation rates and the local Chern marker Eq.(9) is derived within this regime, a proper choice of  $\epsilon$  is essential.

*Local Chern marker in spin models* — By reversing the bosonization procedure, one can express the single-magnon initial state  $|\downarrow_i\rangle$  as well as the perturbation in Eq. (6) in the spin language; this mapping allows one to describe a practical procedure to access the local Chern marker in spin systems through circular dichroism. In the

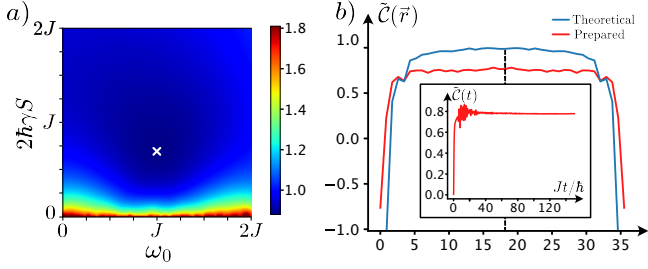


Figure 3. *Driven-dissipative preparation scheme and local Chern marker measurement.* (a) Uniformity factor  $\mathcal{U}$  [Eq. (17)] for the steady-state solution of the mean-field equations [Eq. (S23)], as a function of the pump frequency  $\omega_0$  and the loss rate  $2\hbar\gamma S$ . Its minimal value is marked by a white cross, which is located at  $\hbar\omega_0 = J$  and  $2\hbar\gamma S = 0.695J$ . (b) The local Chern marker  $\tilde{\mathcal{C}}(\vec{r})$ , as obtained from a dichroic measurement performed on the steady state, using the optimal pump-loss parameters [panel (a)]. The marker is displayed along the dashed line represented in Fig. 1(d). At each position, we extracted the long-time limit of the integrated differential rate (inset). The resulting local marker slightly deviates from a quantized value ( $\tilde{\mathcal{C}} \sim 0.8$ ); the marker obtained from the ideal initial state is shown in blue for comparison.

spin language, the equivalent of single-boson states corresponds to states of the magnetization sector  $S_z = NS - 1$  with  $N$  the number of sites and  $S$  the spin amplitude, such that the equivalent of  $|\downarrow_i\rangle$  is given by

$$|\downarrow_i^s\rangle = \frac{\sum_{g \in LB} |g\rangle \langle g|i\rangle}{\sqrt{\sum_{g \in LB} |\langle g|i\rangle|^2}}, \quad \text{with } |i\rangle = \hat{s}_i^- |0\rangle, \quad (12)$$

with  $\hat{s}_j^\pm = \hat{s}_j^x \pm i\hat{s}_j^y$ ,  $|0\rangle$  the ground state defined by  $\hat{s}_i^\pm |0\rangle = 0$  for all sites  $i$ , and where  $|g\rangle$  denotes the eigenstates belonging to the lowest magnon energy band.

Extending the spin-boson mapping to the circular driving, we then consider a chiral perturbation of the form (5) with  $\hat{x}/\hat{y}$  the spin position operators defined through the Holstein-Primakoff transform (2):

$$\hat{x} = \sum_j x_j \hat{a}_j^\dagger \hat{a}_j \rightarrow \hat{x} = - \sum_j x_j \hat{s}_i^z. \quad (13)$$

Here, we made use of the fact that all matrix elements are of the form  $\langle e|x/y|g\rangle$ , where  $|e\rangle$  and  $|g\rangle$  are orthogonal states ( $\langle e|g\rangle = 0$ ), to simplify a constant term.

The numerical study of our local circular-dichroic scheme can be performed at the level of the spin description. We verified that the results are strictly identical to those presented in Fig. 2 for the bosonic model within the present single-magnon framework.

*Initial state preparation* — We now discuss how the single-magnon initial states  $|\downarrow_i\rangle$  introduced above [Eqs. (4),(12)] can be produced in practice, in an experimental context. Historically, it has been proposed that

magnons can be controlled by coupling the system to a metallic layer traversed by an electric current, either globally [32–34] or at the edges [35]; see also Ref. [36] for possible preparation schemes in cold atoms.

Here, we explore a possible scheme that combines a local external pump with the global inherent losses of spin systems [Fig. 1.(c)]. On the one hand, the local pumping is included directly at the Hamiltonian level

$$\delta\hat{\mathcal{H}}_{pump} = \sum_i \mu_B B_i (e^{i\omega_0 t} \hat{s}_i^+ + e^{-i\omega_0 t} \hat{s}_i^-). \quad (14)$$

Such a pumping can be engineered experimentally by coupling the system to an external rotating magnetic field

$$\sum_i \mu_B \vec{B}_i(t) \cdot \vec{S}_i, \quad \vec{B}_i = 2B_i \begin{pmatrix} \cos(\omega_0 t) \\ \sin(\omega_0 t) \\ 0 \end{pmatrix}, \quad (15)$$

with a localized amplitude  $B_j = \delta_{ij}$ , chosen to realize the local excitation  $|\downarrow_i\rangle$ . On the other hand, losses are assumed to be local and uniform for all lattice sites. These losses, associated with random magnon losses (i.e. spin-flip  $\hat{s}_i^+$ ) at a rate  $\gamma$ , are included in the system using a Lindblad master equation formalism [30]. Considering the large  $S$  limit for illustration purposes, and transforming spins to bosons following the Holstein-Primakoff mapping (2), the equation of motion for  $b_i = e^{i\omega_0 t} \langle \hat{a}_i \rangle$  takes the form

$$i\partial_t b_i = -JS \sum_{\langle ij \rangle} (b_i - b_j) - iDS \sum_{\langle\langle ij \rangle\rangle} \eta_{ij} b_j - \sqrt{2S} B_i - (\omega_0 + 2i\gamma S) b_i. \quad (16)$$

We note that similar equations of motion were explored in the context of driven-dissipative photonic lattices [37–39].

Given a pump frequency  $\omega_0$  and a loss rate  $\gamma$ , it is possible to obtain a steady state of Eq. (16),  $\partial_t b_i = 0$ ,  $\forall i$ . The preparation protocol can then be optimized by identifying the parameters that yield a steady state that closely resembles the “ideal” state  $|\downarrow_i^s\rangle$ . The distance to this ideal state can be evaluated by computing the fidelity  $|\langle \psi(t) | \downarrow_i^s \rangle|^2$ ; instead, we monitor the uniformity with which the steady state populates the target band. To do so, we introduce a uniformity factor

$$\mathcal{U} = \sum_{j \in LB} \left| |\langle i_{mf} | j \rangle|^2 - 1/n_{LB} \right|, \quad (17)$$

with  $|i_{mf}\rangle$  the normalized solution to the mean-field equations in the large  $S$  approximation (16), and  $n_{LB} = \sum_{j \in LB} 1$ . Identifying the optimal couple  $(\omega_0, \gamma)$  then implies minimizing this uniformity criterion.

In the ideal scenario where the bandwidth  $W$  of the lowest Bloch band is small compared to the bandgap  $\Delta$ , the optimal preparation scheme consists in choosing  $\omega_0$  in the middle of the lowest band, with a loss rate set

such that  $W \ll \gamma \ll \Delta$ ; see Refs. [37, 38]. In the present case, however, the bands are substantially dispersive, and we find that the uniformity is maximized for a pump frequency  $\hbar\omega_0 \approx J$  and a loss rate  $\hbar\gamma \approx 0.695J$ ; see Fig. 3(a).

A realistic local Chern marker measurement for spin systems would proceed by preparing a localized initial state via this optimal driven-dissipative scheme, followed by the dichroic protocol described above. An illustrative example of the integrated signal is presented in Fig. 3(b). Repeating this locally across all sites maps out the marker, which is homogeneous in the bulk with  $\tilde{\mathcal{C}}(\vec{r}) \approx 0.78$ , and decreasing near the edges. We have verified that this measurement systematically improves with system size, e.g.  $\tilde{\mathcal{C}}(\vec{r}) \approx 0.85$  for a  $30 \times 30$  lattice. Still, inevitable deviations from the ideal state ( $\mathcal{U} < 1$ ) introduce a small residual error in the Chern marker as the system approaches the thermodynamic limit.

Since the residual error is due to an inhomogeneous population of the target band, one could envisage a refined pumping protocol, based on a multi-frequency pulse. Adjusting the bandwidth of the pump would then naturally lead to a uniform population of the band, hence leading to an improvement of the Chern marker measurement.

*Discussion & Perspectives* — This work introduced a strategy to access a local topological marker in bosonic systems, which is based on combining a local driven-dissipative preparation scheme with a circular-dichroic measurement. While this work illustrated this scheme in the context of topological magnons, the recipe described above can be generalized to any spin system with bosonic low-energy excitations. In general, the protocol consists in identifying: (i) a localized single-excitation state; (ii) a suitable driven-dissipative protocol to prepare this local state, while optimizing the uniform filling of the target topological band; and (iii) the chiral perturbation [Eq. (5)], where the position operator takes the form  $\hat{x} = \sum_i x_i \hat{n}_i$ , with  $\hat{n}_i$  the local bosonic densities.

An interesting perspective concerns the physics beyond the single-excitation approximation, which is considered in this work. It would be intriguing to explore the effectiveness of the preparation protocol beyond the classical mean-field theory, but also the effects of magnon-magnon interactions, and the fate of bulk topology in the absence of magnon conservation [14].

Beyond topological Chern bands, other types of topological properties can arise from spin systems, such as magnon (pseudo)-spin Hall states [40, 41] or Majorana fermions in Kitaev-type honeycomb models [42–44]. In this context, our work paves the way to numerical and experimental investigations of real-space topological markers beyond Chern insulators, applicable to spin systems. The strategy described in this work can be generalized depending on the case under study: by including a chiral modulation that depends on both the spin and the sublattice degree of freedom ( $\hat{n}_i = \hat{\tau}_i^z \hat{\sigma}_i^z$ ) in the context of

magnon spin-Hall systems, or by coupling the perturbation to the density of Majorana fermions in the case of the Kitaev honeycomb model.

We acknowledge Marco Schiro, Marin Bukov, Antoine Georges and Johannes Knolle for useful discussions. This work was supported by the ERC (LATIS project), the EOS project CHEQS, and the Fondation ULB. We used Quspin for simulating the dynamics of the magnons and spin systems [45, 46]

---

\* baptiste.bermond@lkb.ens.fr

† anais.defossez@lkb.ens.fr

‡ nathan.goldman@lkb.ens.fr

- [1] X. Cao, K. Chen, and D. He, *Journal of Physics: Condensed Matter* **27**, 166003 (2015).
- [2] S. A. Owerre, *Journal of Physics: Condensed Matter* **28**, 386001 (2016).
- [3] P. A. McClarty, *Annual Review of Condensed Matter Physics* **13**, 171 (2022).
- [4] S. Subramanian, T. Berlijn, L. Lindsay, R. S. Fishman, and J. W. Villanova, “Topological magnons on the ferromagnetic zigzag lattice,” (2024), arXiv:2411.18515.
- [5] F. Zhuo, J. Kang, A. Manchon, and Z. Cheng, *Advanced Physics Research* **4**, 2300054 (2025).
- [6] R. Chisnell, J. S. Helton, D. E. Freedman, D. K. Singh, R. I. Bewley, D. G. Nocera, and Y. S. Lee, *Phys. Rev. Lett.* **115**, 147201 (2015).
- [7] M. Hirschberger, R. Chisnell, Y. S. Lee, and N. P. Ong, *Phys. Rev. Lett.* **115**, 106603 (2015).
- [8] Y. Miura, R. Hirai, Y. Kobayashi, and M. Sato, *Journal of the Physical Society of Japan* **75**, 084707 (2006).
- [9] A. A. Tsirlin, O. Janson, and H. Rosner, *Phys. Rev. B* **82**, 144416 (2010).
- [10] M. dos Santos Dias, N. Biniskos, F. Dos Santos, K. Schmalzl, J. Persson, F. Bourdarot, N. Marzari, S. Blügel, T. Brückel, and S. Lounis, *Nature Communications* **14**, 7321 (2023).
- [11] L. Chen, J.-H. Chung, B. Gao, T. Chen, M. B. Stone, A. I. Kolesnikov, Q. Huang, and P. Dai, *Physical Review X* **8**, 041028 (2018).
- [12] D. Malz, J. Knolle, and A. Nunnenkamp, *Nature communications* **10**, 3937 (2019).
- [13] J. Feldmeier, W. Natori, M. Knap, and J. Knolle, *Physical Review B* **102**, 134423 (2020).
- [14] J. Habel, A. Mook, J. Willsher, and J. Knolle, *Physical Review B* **109**, 024441 (2024).
- [15] R. Bianco and R. Resta, *Physical Review B—Condensed Matter and Materials Physics* **84**, 241106 (2011).
- [16] R. Bianco and R. Resta, *Phys. Rev. Lett.* **110**, 087202 (2013).
- [17] R. Umucalılar, H. Zhai, and M. Oktel, *Physical review letters* **100**, 070402 (2008).
- [18] C. Repellin, J. Léonard, and N. Goldman, *Phys. Rev. A* **102**, 063316 (2020).
- [19] B. Wang, M. Aidelsburger, J. Dalibard, A. Eckardt, and N. Goldman, *Physical review letters* **132**, 163402 (2024).
- [20] A. Markov, D. Golovanova, A. Yavorsky, and A. Rubtsov, *SciPost Physics* **17**, 152 (2024).
- [21] D. T. Tran, A. Dauphin, A. G. Grushin, P. Zoller, and

- N. Goldman, *Science advances* **3**, e1701207 (2017).
- [22] C. Repellin and N. Goldman, *Physical review letters* **122**, 166801 (2019).
- [23] L. Asteria, D. T. Tran, T. Ozawa, M. Tarnowski, B. S. Rem, N. Fläschner, K. Sengstock, N. Goldman, and C. Weitenberg, *Nature physics* **15**, 449 (2019).
- [24] N. Goldman and T. Ozawa, *Comptes Rendus. Physique* **25**, 289 (2024).
- [25] P. Mognini, B. Lapiere, R. Chitra, and W. Chen, *SciPost Phys. Core* **6**, 059 (2023).
- [26] S. K. Kim, H. Ochoa, R. Zarzuela, and Y. Tserkovnyak, *Physical review letters* **117**, 227201 (2016).
- [27] T. Moriya, *Physical review* **120**, 91 (1960).
- [28] Y. H. Gao, C. Hickey, T. Xiang, S. Trebst, and G. Chen, *Physical Review Research* **1**, 013014 (2019).
- [29] T. Holstein and H. Primakoff, *Physical Review* **58**, 1098 (1940).
- [30] The Supplemental Material includes a description of the Holstein-Primakoff transform, a discussion of time-dependent perturbation theory and its numerical limitations, a discussion of the mapping of the position operators in the spin language as well as a discussion of the Lindblad master equation in the context of homogeneous losses in the material.
- [31] F. D. M. Haldane, *Physical review letters* **61**, 2015 (1988).
- [32] L. Berger, *Physical Review B* **54**, 9353 (1996).
- [33] J. C. Slonczewski, *Journal of Magnetism and Magnetic Materials* **159**, L1 (1996).
- [34] P. M. Gunnink, R. A. Duine, and A. Mook, *Physical Review B* **110**, 014407 (2024).
- [35] S. Lee, G. Go, and S. K. Kim, *Physical Review B* **107**, 144423 (2023).
- [36] F. Mei, G. Chen, N. Goldman, L. Xiao, and S. Jia, *New Journal of Physics* **21**, 095002 (2019).
- [37] T. Ozawa and I. Carusotto, *Physical review letters* **112**, 133902 (2014).
- [38] T. Ozawa, H. M. Price, N. Goldman, O. Zilberberg, and I. Carusotto, “Synthetic dimensions in integrated photonics: From optical isolation to four-dimensional quantum hall physics,” (2016).
- [39] A. Chénier, B. d’Aligny, F. Pellerin, P. Édouard Blanchard, T. Ozawa, I. Carusotto, and P. St-Jean, “Quantized hall drift in a frequency-encoded photonic chern insulator,” (2024), arXiv:2412.04347.
- [40] H. Kondo, Y. Akagi, and H. Katsura, *Physical Review B* **99**, 041110 (2019).
- [41] E. Viñas Boström, T. S. Parvini, J. W. McIver, A. Rubio, S. V. Kusminskiy, and M. A. Sentef, *Physical Review Letters* **130**, 026701 (2023).
- [42] A. Kitaev, *Annals of Physics* **321**, 2 (2006).
- [43] B.-Y. Sun, N. Goldman, M. Aidelsburger, and M. Bukov, *PRX Quantum* **4**, 020329 (2023).
- [44] E. Koller, V. Leeb, N. B. Perkins, and J. Knolle, “Raman circular dichroism and quantum geometry of chiral quantum spin liquids,” (2025), arXiv:2503.14091.
- [45] P. Weinberg and M. Bukov, *SciPost Phys.* **2**, 003 (2017).
- [46] P. Weinberg and M. Bukov, *SciPost Phys.* **7**, 020 (2019).

## SUPPLEMENTAL MATERIAL

### A local quantized marker for topological magnons from circular dichroism

#### SPIN WAVES, AND HOLSTEIN-PRIMAKOFF TRANSFORM

A standard way to describe magnonic excitations above an ordered ground state is to map the spin operators to bosonic operators using a so-called Holstein–Primakoff transformation [S1]. Assuming as in the main text that the ground-state is polarized in the z-direction, the Holstein Primakoff transform takes the form (2)

$$\hat{s}_i^+ = \sqrt{2S} \sqrt{1 - \frac{\hat{a}_i^\dagger \hat{a}_i}{2S}} \hat{a}_i, \quad (\text{S1})$$

$$\hat{s}_i^- = \sqrt{2S} \hat{a}_i^\dagger \sqrt{1 - \frac{\hat{a}_i^\dagger \hat{a}_i}{2S}}, \quad (\text{S2})$$

$$\hat{s}_i^z = S - \hat{a}_i^\dagger \hat{a}_i, \quad (\text{S3})$$

where  $\hat{a}_i^\dagger$  ( $\hat{a}_i$ ) creates(/annihilates) a magnon at site  $i$ . Plugging this transform into the Hamiltonian (1) and performing a large- $S$  expansion, the Hamiltonian becomes a power series in  $1/S$

$$\hat{\mathcal{H}} = E_{GS} + \hat{\mathcal{H}}_2 + \hat{\mathcal{H}}_3 + \hat{\mathcal{H}}_4 + O(S^{-3/2}), \quad (\text{S4})$$

where  $E_{GS}$  is the ground state energy, while the operator  $\hat{\mathcal{H}}_n$  is of order  $S^{2-n/2}$  and contains  $n$  bosonic operators. The quadratic component  $\hat{\mathcal{H}}_2$  is called the linear spin wave Hamiltonian and reads

$$\hat{\mathcal{H}}_2 = -JS \sum_{\langle ij \rangle} \left( \hat{a}_j^\dagger \hat{a}_i + \hat{a}_i^\dagger \hat{a}_j \right) + JS \sum_i z_i \hat{a}_i^\dagger \hat{a}_i + iDS \sum_{\langle\langle ij \rangle\rangle} \eta_{ij} \left( \hat{a}_j^\dagger \hat{a}_i - \hat{a}_i^\dagger \hat{a}_j \right). \quad (\text{S5})$$

Higher order terms in the series expansion encode many-body magnon-magnon interactions beyond the linear spin wave picture. In the specific case of a ground state polarized along the z-axis, since the magnetization is conserved,

all odd-order term ( $\hat{\mathcal{H}}_{2n+1}$ ) are equal to 0, and all even-order terms ( $\hat{\mathcal{H}}_{2n}$ ) have the same number of creation and annihilation operators. As a consequence, magnon-magnon interaction processes ( $\hat{\mathcal{H}}_n, n > 2$ ) are strictly absent in the single- magnon regime.

## TIME-DEPENDENT PERTURBATION THEORY AND NUMERICAL LIMITATIONS

In this section of the supplemental materials, we revisit time-dependent perturbation theory and circular dichroism to derive Eqs. (6) and (8) employed in the main text.

### Time-dependent perturbation theory

Let us consider a Hamiltonian  $\hat{\mathcal{H}}_0$  of eigenstates  $|n\rangle$ , such that  $\hat{\mathcal{H}}_0|n\rangle = E_n|n\rangle = \hbar\omega_n|n\rangle$ , and a time-dependent perturbation of the form

$$\delta\hat{\mathcal{H}}_\chi(t) = 2\epsilon [\hat{x} \cos(\omega t) + \chi\hat{y} \sin(\omega t)]. \quad (\text{S6})$$

To proceed, we express the system's wavefunction in the interaction picture in the form

$$|\Psi(t)\rangle = \sum_n c_n(t) e^{-i\omega_n t} |n\rangle, \quad (\text{S7})$$

such that the Schrödinger equation

$$i\hbar\partial_t |\Psi(t)\rangle = (\hat{\mathcal{H}}_0 + \delta\hat{\mathcal{H}}_\chi(t)) |\Psi(t)\rangle \quad (\text{S8})$$

projected onto the eigenstates of  $\hat{\mathcal{H}}_0$  takes the form

$$i\hbar\partial_t c_n(t) = \sum_m c_m(t) e^{-i(\omega_m - \omega_n)t} \langle n | \delta\hat{\mathcal{H}}_\chi(t) | m \rangle, \quad \forall n. \quad (\text{S9})$$

At linear order in  $\epsilon$  in perturbation theory, the coefficients  $c_n(t)$  are given by

$$c_n(t) = c_n(0) + \epsilon \sum_m c_m(0) \left( \frac{e^{-i(\omega_m - \omega_n - \omega)t} - 1}{E_m - E_n - \hbar\omega} \langle n | \hat{x} - i\chi\hat{y} | m \rangle + \frac{e^{-i(\omega + \omega_m - \omega_n)t} - 1}{E_m - E_n + \hbar\omega} \langle n | \hat{x} + i\chi\hat{y} | m \rangle \right). \quad (\text{S10})$$

Assuming, as in the main text, that the system is initialized in a state  $|\psi_0\rangle$  at  $t = 0$  such that only the lowest band is occupied (*i.e.*  $\forall n \notin LB, c_n(0) = \langle n | \psi_0 \rangle = 0$ ), the density of particles in the higher bands corresponds to the number of excited particles from the lowest bands to the others between times 0 and  $t$ . It satisfies

$$\begin{aligned} N^\pm(\omega, t) &= \sum_{n \notin LB} |c_n(t)|^2 \\ &= \epsilon^2 \sum_{n \notin LB} \left| \sum_{m \in LB} c_m(0) \left( \langle n | \hat{x} \mp i\hat{y} | m \rangle \frac{e^{-it(\omega_m - \omega_n - \omega)} - 1}{E_m - E_n - \hbar\omega} + \langle n | \hat{x} \pm i\hat{y} | m \rangle \frac{e^{-it(\omega_m - \omega_n + \omega)} - 1}{E_m - E_n + \hbar\omega} \right) \right|^2. \end{aligned} \quad (\text{S11})$$

Under a rotating wave approximation, valid in the regime  $\omega t \gg 2\pi$ , and given that  $\omega_m < \omega_n$ , the number of particles in the excited states then reads

$$N^\pm(\omega, t) = \left( \frac{\epsilon}{\hbar} \right)^2 \sum_{n \notin LB} \left| \sum_{m \in LB} \langle n | \hat{x} \pm i\hat{y} | m \rangle \langle m | \psi_0 \rangle \frac{e^{it(\omega_n - \omega_m - \omega)} - 1}{\omega_n - \omega_m - \omega} \right|^2, \quad (\text{S12})$$

which is identical to Eq. (6) in the main text.

### Circular dichroism and local Chern marker

Because we consider an initial state localized in position  $|\psi_0\rangle$ , its occupations in the lowest band states  $\langle m|\psi_0\rangle$ ,  $\{m \in LB\}$ , are correlated, leading to interferences between eigenstates of different energies. Contrary to the usual Fermi golden rule or to other works dedicated to dichroism [S2, S3], it is consequently impossible to extract information directly from a single frequency measurement. One can get rid of these interferences by integrating the excitation rates  $N_{\pm}(\omega, t)/t$  over all relevant frequencies. Using the limit,

$$\frac{1}{t} \int \frac{e^{it(\omega_1-\omega)} - 1}{\omega_1 - \omega} \frac{e^{-it(\omega_2-\omega)} - 1}{\omega_2 - \omega} d\omega \xrightarrow{t \rightarrow +\infty} 2\pi\delta_{\omega_1, \omega_2}, \quad (\text{S13})$$

valid for  $t \gg \frac{2\pi}{\omega_1 - \omega_2}$ , one gets

$$\int d\omega \Gamma^{\pm}(\omega, t) \xrightarrow{t \rightarrow +\infty} \frac{2\pi\epsilon^2}{\hbar^2} \sum_{e \notin LB} \sum_{g \in LB} |\langle e|\hat{x} \pm i\hat{y}|g\rangle|^2 |\langle g|\psi_0\rangle|^2, \quad (\text{S14})$$

such that the difference of the chiral excitation rates reads

$$\begin{aligned} \int d\omega (\Gamma^+(\omega, t) - \Gamma^-(\omega, t)) &\xrightarrow{t \rightarrow +\infty} -\frac{8\pi\epsilon^2}{\hbar^2} \text{Im} \left( \sum_{e \notin LB} \sum_{g \in LB} |\langle \psi_0|g\rangle|^2 \langle g|\hat{x}|e\rangle \langle e|\hat{y}|g\rangle \right) \\ &\xrightarrow{t \rightarrow +\infty} -\frac{8\pi\epsilon^2}{\hbar^2} \text{Im} \left( \sum_{g \in LB} \langle \psi_0|g\rangle \langle g|\hat{x}\hat{Q}\hat{y}|g\rangle \langle g|\psi_0\rangle \right), \end{aligned} \quad (\text{S15})$$

where  $\hat{Q}$  is the projector onto the highest bands  $\hat{Q} = \sum_{e \notin LB} |e\rangle \langle e|$ , recovering Eq. (8) of the main text.

### Limitations of the time-dependent perturbation theory analysis

We aim here to review the various assumptions necessary to justify the link between the local quantized Chern marker and the differential integrated excitation rate, as expressed in Eqs. (8) and (9), within the framework of linear response theory.

We first validate, as shown in Fig. S1(b), that the first order approximation of the perturbative expansion in  $\epsilon$  of the excited density particles holds for times  $t$  such that, for any initial state in the lowest band, the condition  $\epsilon t \ll |\langle e|\hat{x} \pm i\hat{y}|g\rangle|$  is fulfilled. When we loosen this hypothesis, the integrated differential excitation rate  $\Delta\Gamma$  tends to decrease in the long-time limit. Additionally, Fig. S1(c) illustrates that both chiral excitation rates  $\Gamma_{i,\pm}(t)$  reach a constant value when the time  $t$  is fixed and  $\epsilon$  remains below a critical value  $\epsilon_c \sim \frac{1}{t} \min(|\langle e|\hat{x} \pm i\hat{y}|g\rangle|)$ .

Moreover, the integral is approximated by a finite sum, with a frequency step  $\Delta\omega$ , as is done in any reasonable numerical or experimental situation. Such an approximation, however, only holds when  $t$  satisfies  $\Delta\omega t \ll 2\pi$ . This constraint is exemplified in Fig. S1(d), where we observe that the curves obtained for larger values of  $\Delta\omega$  begin to deviate from the others around  $2\pi/\Delta\omega$ , indicated by the dashed line. One must therefore balance the three key timescales imposed by (i) the measurement duration, (ii) the finite perturbation strength  $\epsilon$ , and (iii) the energy resolution we wish to probe, as described in (S13). Achieving finer energy resolution requires longer measurement times, which in turn necessitates smaller excitation amplitudes and a greater number of measurements across different frequencies.

### Position operator in the spin language

In the bosonic language, position operators  $\hat{x}/\hat{y}$  take the simple form

$$\hat{x} = \sum_i x_i \hat{a}_i^\dagger \hat{a}_i \quad (\text{S16})$$

with  $x_i$  the  $x$ -coordinate of site  $i$ . To translate these operators in the spin language several proposals have been made:

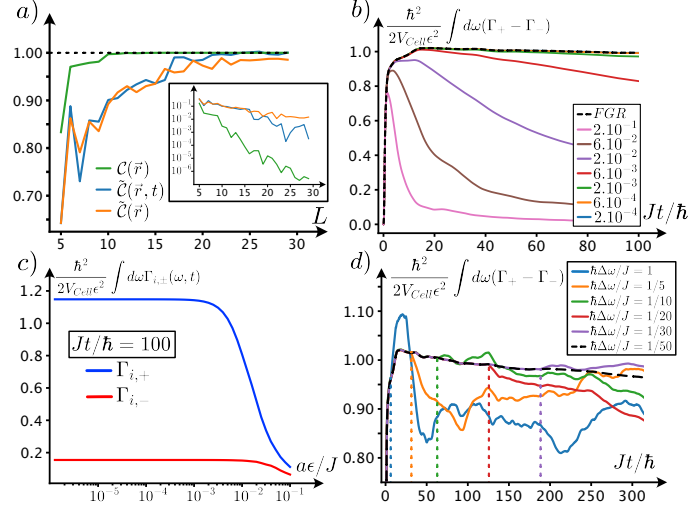


Figure S1. *Limitations of the local Chern markers.* (a) Finite-size analysis of the three types of local Chern markers discussed in the article: we compare the standard local Chern marker introduced by Bianco and Resta in [S4] [Eq. (10)] (green), the finite time estimation of the local Chern marker introduced in this work  $\tilde{C}(\vec{r}, t)$  at  $Jt/\hbar = 100$  (blue), and its long-time limit  $\lim_{t \rightarrow \infty} \tilde{C}(\vec{r}, t)$  (orange) [Eq. (9)], as functions of the system size. The inset shows the same data on a semi-logarithmic scale to highlight the exponential convergence of the markers. (b) Time evolution of the integrated differential rate [Eq. (8)] for different perturbation amplitudes  $\epsilon$ . As  $\epsilon$  decreases, the dynamics converge toward the value predicted by Fermi's golden rule, represented in dashed lines. (c) The integrated chiral excitation rates  $\int d\omega\Gamma^{\pm}(\omega, t)$  at  $Jt/\hbar = 100$  are shown as functions of the excitation amplitude  $a\epsilon/J$ . (d) Time evolution of the integrated differential rate [Eq. (8)] displayed for several integration steps  $\Delta\omega$ . The curves with larger  $\Delta\omega$  begin to deviate from the ideal integral ( $\sim \Delta\omega \rightarrow 0$ ) around  $Jt/\hbar = 2\pi/\Delta\omega$ , as marked by the vertical dashed lines.

- A first idea, used in the main text is to make use of the Holstein-Primakoff transform of  $\hat{s}^z$  to rewrite the position operator as

$$\hat{x} = \sum_i x_i (S - \hat{s}_i^z) \quad (\text{S17})$$

Since all the matrix element involved in the Fermi golden rule are of the form  $\langle e|\hat{x}|g\rangle$ , involving two orthogonal states  $|e\rangle$  and  $|g\rangle$ , the expression of the position operator (S17) can be simplified to  $\hat{x} = -\sum_i x_i \hat{s}_i^z$ . It is however important to note that beyond the ideal limit in which only state belonging to the lowest band are excited at  $t = 0$ , such a simplification would fail and require one to go back to the full expression (S17).

- Alternatively, developing the Holstein-Primakoff transform at first order in  $1/S$ , one could be tempted to map “ $\hat{a}_i^\dagger \rightarrow \hat{s}_i^-$ ” and “ $\hat{a}_i \rightarrow \hat{s}_i^+$ ”, and use a modified position operator of the form [S5]

$$\hat{x} = \frac{1}{2S} \sum_j x_j \hat{s}_j^- \hat{s}_j^+. \quad (\text{S18})$$

However, from the spin algebra  $\hat{s}^- \hat{s}^+ = S(S+1)\hat{\mathbb{1}} - (\hat{s}^z)^2 - \hat{s}^z$ , one realizes that the replacement  $\hat{a}^\dagger \hat{a} \rightarrow \hat{s}^- \hat{s}^+$  is only valid in two limits: First, for spin-1/2 particles, we indeed have  $\hat{s}^- \hat{s}^+ = \frac{1}{2} - \hat{s}^z$ , since  $(\hat{s}^z)^2 = S^2 \hat{\mathbb{1}}$ ; and second, in the large S limit, since  $\frac{1}{2S} \hat{s}^- \hat{s}^+ = \hat{a}^\dagger \hat{a} - \frac{\hat{a}^\dagger \hat{a}^\dagger \hat{a} \hat{a}}{2S} \approx \hat{a}^\dagger \hat{a}$ .

## INITIAL STATE PREPARATION

In this section, we will first review the theoretical tools leading to the mean-field equations in the presence of both losses and pumping used in the main text for the initial state preparation. In order to describe the loss rate in the spin system, we resort to a Lindblad master equation for the reduced density

matrix  $\hat{\rho}$  [S6, S7]

$$i\hbar\partial_t\hat{\rho} = [\hat{\mathcal{H}}, \hat{\rho}] + i\hbar \sum_k 2\gamma_k \left( \hat{L}_k \hat{\rho} \hat{L}_k^\dagger - \frac{1}{2} \{ \hat{L}_k^\dagger \hat{L}_k, \hat{\rho} \} \right), \quad (\text{S19})$$

with  $\hat{\mathcal{H}}$  the total Hamiltonian of the system with pumping at a frequency  $\omega_0$

$$\hat{\mathcal{H}} = -J \sum_{\langle ij \rangle} \vec{s}_i \cdot \vec{s}_j + \sum_{\langle\langle ij \rangle\rangle} \vec{D}_{ij} \cdot (\vec{s}_i \wedge \vec{s}_j) + \sum_i \mu_B B_i (e^{i\omega_0 t} \hat{s}_i^+ + e^{-i\omega_0 t} \hat{s}_i^-), \quad (\text{S20})$$

and where  $\hat{L}_k$  denotes a set of jump operators in our case given by  $\hat{L}_k = \hat{s}_k^+$ . Assuming, as in the main text, homogeneous losses in the overall system ( $\gamma_k \equiv \gamma$ ), each operator  $\hat{\mathcal{O}}$  in the Heisenberg picture evolves as

$$i\hbar\partial_t\hat{\mathcal{O}} = [\hat{\mathcal{H}}, \hat{\mathcal{O}}] + i\hbar \sum_k 2\gamma_k \left( \hat{L}_k \hat{\mathcal{O}} \hat{L}_k^\dagger - \frac{1}{2} \{ \hat{L}_k^\dagger \hat{L}_k, \hat{\mathcal{O}} \} \right). \quad (\text{S21})$$

As a consequence, the Heisenberg equations for the spin operators  $\hat{s}_i^z/\hat{s}_i^\pm$  read

$$i\hbar\partial_t\hat{s}_i^z = [\hat{\mathcal{H}}, \hat{s}_i^z] + 2i\hbar\gamma\hat{s}_i^-\hat{s}_i^+, \quad (\text{S22a})$$

$$i\hbar\partial_t\hat{s}_i^\pm = [\hat{\mathcal{H}}, \hat{s}_i^\pm] - 2i\hbar\gamma\hat{s}_i^z\hat{s}_i^\pm. \quad (\text{S22b})$$

leading to the mean-field equations

$$i\partial_t s_i^z = -\frac{J}{2} \sum_{\langle ij \rangle} (s_i^+ s_j^- - s_i^- s_j^+) + \frac{iD}{2} \sum_{\langle\langle ij \rangle\rangle} \eta_{ij} (s_i^+ s_j^- + s_i^- s_j^+) + B_i (e^{i\omega_0 t} s_i^+ - e^{-i\omega_0 t} s_i^-) + 2i\gamma s_i^- s_i^+, \quad (\text{S23a})$$

$$\pm i\partial_t s_i^\pm = -J \sum_{\langle ij \rangle} (-s_i^\pm s_j^z + s_i^z s_j^\pm) \mp iD \sum_{\langle\langle ij \rangle\rangle} \eta_{ij} s_i^z s_j^\pm + 2B_i e^{\mp i\omega_0 t} s_i^z \mp 2i\gamma s_i^z s_i^\pm, \quad (\text{S23b})$$

where  $s_i^z = \langle \hat{s}_i^z \rangle$  and  $s_i^\pm = \langle \hat{s}_i^\pm \rangle$ .

Working in the rotating wave picture around the z-axis, setting  $\sigma_i^\pm = e^{\pm i\omega_0 t} s_i^\pm$ , mean-field equations (S23) can be expressed as

$$i\partial_t \sigma_i^z = -\frac{J}{2} \sum_{\langle ij \rangle} (\sigma_i^+ \sigma_j^- - \sigma_i^- \sigma_j^+) + \frac{iD}{2} \sum_{\langle\langle ij \rangle\rangle} \eta_{ij} (\sigma_i^+ \sigma_j^- + \sigma_i^- \sigma_j^+) + B_i (\sigma_i^+ - \sigma_i^-) + 2i\gamma \sigma_i^- \sigma_i^+, \quad (\text{S24a})$$

$$\pm i\partial_t \sigma_i^\pm = -J \sum_{\langle ij \rangle} (-\sigma_i^\pm \sigma_j^z + \sigma_i^z \sigma_j^\pm) \mp iD \sum_{\langle\langle ij \rangle\rangle} \eta_{ij} s_i^z \sigma_j^\pm + 2B_i s_i^z - (\omega_0 \pm 2i\gamma s_i^z) \sigma_i^\pm. \quad (\text{S24b})$$

---

\* baptiste.bermond@lkb.ens.fr

† anais.defossez@lkb.ens.fr

‡ nathan.goldman@lkb.ens.fr

[S1] T. Holstein and H. Primakoff, *Physical Review* **58**, 1098 (1940).

[S2] T. Ozawa and N. Goldman, *Physical Review B* **97**, 201117 (2018).

[S3] C. Repellin and N. Goldman, *Physical review letters* **122**, 166801 (2019).

[S4] R. Bianco and R. Resta, *Physical Review B—Condensed Matter and Materials Physics* **84**, 241106 (2011).

[S5] T. Ozawa and N. Goldman, *Physical Review Research* **1**, 032019 (2019).

[S6] H.-P. Breuer and F. Petruccione, *The theory of open quantum systems* (OUP Oxford, 2002).

[S7] D. Manzano, *AIP Advances* **10**, 025106 (2020).